PARAMETERS CRITICAL TO THE MORPHOLOGY OF FLUIDIZATION CRATERS

BARRY S. SIEGAL and DAVID P. GOLD*
Dept. of Geosciences, The Pennsylvania State University, University Park, Pa., U.S.A.

(Received 20 November, 1972)

Abstract. The anomalously high number of craters with diameter less than 2.8 km, the igneous nature of rocks from the Apollo landing sites, and the possibility of outgassing magmas in the lunar crust, suggest that fluidization may be a viable mechanism for producing many of the smaller lunar craters. Fluidization craters were formed in the laboratory by blowing gas through various thicknesses of particulate material. Gas pressure, 'regolith' thickness, and the duration of gas streaming were controlled over practical experimental limits and compared with the resultant crater morphology. Low to moderate fluidization pressures on 'coarsely' crushed limestone ($M_\phi = 0.40$, $So = 0.50$) with low cohesion ($\phi = 43°$) produced bowl shaped, basin shaped, and flat bottomed craters. Bowl shaped craters change into basin shaped and/or flat bottomed craters with long durations of gas streaming. Cone, funnel, and flat-funnel shaped craters are indicative of high fluidization pressures. Craters formed in 'finely' crushed limestone ($M_\phi = 1.55$, $So = 0.85$) that is electrostatically charged by the streaming gas, are flat bottomed. Terraced craters develop from slumping during and after the discontinuation of gas flow. Central mounds in terraced craters result from slumping into a confined space. In particulate material, fluidization craters have high circularity and axial symmetry, similar to those produced by impact. The use of an impact model and crater morphology ('normal', 'flat bottomed', and 'concentric') for estimating lunar regolith depth is questioned because similar craters can be produced by fluidization processes in a thicker regolith.

1. Introduction

Craters on the Moon smaller than 2.8 km in diameter are believed to be primary, secondary, and endogenic in origin (Kuiper, 1965; Shoemaker, 1965), whereas, larger craters are thought to be impact generated. The anomalously high number of craters with a diameter of 2.8 km or smaller in Mare Tranquillitatis, for example, is unexplainable by the present-day meteorite flux rate (Hartmann, 1970). The origin of several lunar features appears to be volcanic (Green, 1965; McCauley, 1967) with the indication that some specifically are the result of the venting of gas along fractures (Baldwin, 1963; Emmons, 1965; Fielder, 1965; Schumm and Simmons, 1969; Schumm, 1970). Alphonsus, photographed by Ranger IX, displayed large number of 'structurally aligned rimless craters' and low rim craters surrounded by dark halos (McCauley, 1967). In addition, craters between a kilometer and 100 m in diameter were more abundant in maria areas of equal size, and suggests that the floor of Alphonsus is either much older than the maria or that internal cratering processes have been operative; alignment suggests structural control and endogenic processes (McCauley, 1967). The spectrographic evidence of gaseous discharge from the summit of the central mountain in Alphonsus and Aristarchus (Kozyrev, 1959, 1963) also supports

* On leave at the Earth Physics Branch, Dept. of Energy, Mines and Resources, Ottawa, Canada.

The Moon **6** (1973) 304–336.

a theory of lunar degassing*. The Apollo 14 SIDE Mass Analyzer detected 48.6 eV of water vapor ions with a maximum intensity of ~ 107 ions $cm^{-2}\ s^{-1}\ sr^{-1}$ during a 14-h period on March 7, 1971, these are interpreted to be of lunar origin (Freeman *et al.*, 1972a, b). If the igneous rocks from the Apollo sites crystallized from magmas analogous to terrestrial basaltic magmas, then the potential ingredients are present, especially if there is a thick 'regolith' for outgassing and the production of fluidization craters.

The response of the host (or target) material to the cratering process is important in determining the morphology and symmetry of the resulting deformation, and this will vary with the strain rate of the process. By virtue of the extremely high strain rate and hydrodynamic shock state induced by a hypervelocity impact, lateral physical inhomogeneities in the target material are minimized and the resulting deformation will have axial symmetry and high circularity. In contrast, endogenic events involving slower strain rates are strongly influenced by the pre-existing fabric and will reflect this by deviations in circularity and axial symmetry. However, fluidization craters formed in particulate material with little or no horizontal cohesion gradients and of sufficient thickness to support a 'spouting bed' condition, should have a highly developed axial symmetry and circularity (see Plates 2 and 3, and experimental results of Emmons, 1965; Mills, 1969; Schumm, 1970; Siegal, 1971). Thus regardless of their origin, the presence of a thick layer of particulate material (regolith) is an important factor in determining crater morphology. Conversely, crater morphology may be a useful indicator of the thickness of such a layer, provided the mechanism is known.

Almost 20 yr before the *in situ* documentation of a low cohesive, particulate lunar regolith by the Luna, Surveyor, and Apollo missions, radar echos had indicated a loose material of increasing compaction to a significant depth (Kopal, 1970). Estimates of the thickness of this layer (Jaffe, 1965; Shoemaker *et al.*, 1968; Tyler, 1968; Oberbeck and Quaide, 1967, 1968; Quaide and Oberbeck, 1968; Kopal, 1970; Short and Forman, 1972; Siegal and Gold, 1972; Watkins and Kovach, 1972) vary:

(a) Jaffe (1965) suggests that the 'soft' appearance of the lunar craters is due to deposition of granular material and dust after the craters were formed but does not take into account the nature of the target material. Laboratory craters with a 'hard' appearance were overlain by various thicknesses of sand and matched in appearance to lunar craters, 3–13000 m in diameter. On the assumption that a match indicated equal depth of overlay as percentage of crater dimensions, Jaffe (1965) calculated the depth of overlay outside each lunar crater from the laboratory model and the lunar crater dimensions. A minimum depth of 5 m is indicated for the Mare Cognitum area studied.

(b) Shoemaker *et al.* (1968) proposed that the upper crater diameter limit of a steady-state population can be used to deduce regolith thicknesses. Their experimental studies indicate empirically that the upper crater limit size is thirty times larger than

* E. J. Öpik (1971) has interpreted Kozyrev's phenomenon as a solid surface emission, probably fluorescent, and not from an expanding gas.

the size limit for craters whose aggregate area would just cover the surface. Regolith depth corresponds to the depth of the lower size limit craters. Using an upper limit crater diameter of 3 m for the steady state distribution at the Surveyor 7 site Shoemaker *et al.*, (1969) deduced a mean regolith thickness of 9 cm.

(c) Tyler (1968) on the basis of quasi-specular bistatic-radar measurements of the oblique scattering properties of the lunar surface, suggests that the differences in the reflectivity of the maria and highlands may be directly related to regolith depth. Davis and Rohlfs (1964) found that the effective dielectric constant of the lunar surface remained subnormal for signals up into the 15–18 m range, which led Kopal (1970) to deduce a loose regolith to a depth of at least 50–100 m.

(d) Based upon laboratory studies of impact of a projectile into varying thicknesses of loose, granular, low cohesive materials, overlying cohesive substrates, Oberbeck and Quaide (1967) have shown that the realms of crater morphology is dependent upon the ratio of the apparent crater diameter to the surficial layer thickness. Thus, normal, concentric, and flat-bottomed craters (with or without central mounds) with equivalent diameters form within specific fragmental (regolith) thicknesses.

(e) From the distribution of boulders in rille floors, and the traces of rolled boulders on rille walls, Kopal (1970) reasoned that the sinuous rilles (at least those lacking flat floors) are cut in loose cosmic abrasion debris (regolith) and indicate minimum regolith depths of 200–300 m in the vicinity of the Bode, Prinz, and Hadley rilles. The flat floored rilles may indicate proximity to bedrock, which in Schroeter's Canyon would be about 840 m deep.

(f) Short and Forman (1972) suggest the volume of ejected material from craters and basins between 3.5 and 500 km diameter on the visible face of the Moon would create an average regolith thickness between 0.74 and 8.00 km. The value depends upon the combination of critical parameters used, and as a best estimate is between 1.36–2.39 km.

(g) The Apollo 14 Active Seismic Experiments indicates a loose surficial layer 8.5 m thick on the Fra Mauro Formation ejecta blanket (16–76 m thick) which in turn overlies material (probably ejecta) with P wave velocities of 370 m s^{-1} (Watkins and Kovach, 1972).

Lunar morphological features have been simulated in fluidized beds (Emmons, 1965; Mills, 1969; Schumm, 1970; Siegal, 1971; Siegal and Gold, 1972). Emmons (1965) showed that the gentle rim slopes, the steep interior slopes, slumps, faults, terraces, central cones, and interior craterlets associated with many lunar craters could be duplicated in laboratory craters formed by streaming gas. Mill's (1969) experimental studies of the development of circular features on a slowly collapsing fluidized bed showed that the criterion of a comparatively gentle mode of origin for multiple craters was satisfied. Schumm (1970) performed experiments to determine the morphology of the resulting features when varying thicknesses of particulate material was fluidized from vents of various sizes and configurations.

To further examine the role of fluidization on the Moon, a laboratory investigation was undertaken on two particulate material size fractions to determine the effect

of variables, such as, duration of gas streaming, gas pressure, and 'regolith' thickness on the morphology of fluidization craters. A 3.175–mm cylindrical vent was used to simulate a gas streaming conduit; the significance of various diameters and vent configurations on the morphology of the resulting crater is left for future studies.

2. Fluidization Chamber, and Experimental Control

A fluidization chamber consisting of three sections (Plate 1) was built out of 12.7 mm thick transparent plexiglass. The lower section is an air tight rectangular chamber with an interchangeable top, a template. Two connectors were tapped into opposite walls of the chamber, one for ingress of gas from a high pressure cylinder, and the other for a pressure gauge coupling, to measure the gas pressure in the chamber. The 6.35 mm thick plexiglass template was overlain by an 1.59 mm thick felt to prevent the passage of the particulate material through the vent when the chamber was not in use. The upper section of the fluidization chamber is a rectangular shaped column.

Bottled nitrogen gas was selected as a dry homogeneous source of inert gas of uniform density and was bled through a Hoke Regulator into the lower chamber. The chamber pressure was measured with a Reid Vapor Gauge, and a mercury manometer.

To minimize adherence of the very fine particulate material in the fluidization chamber the relative humidity of the room was controlled to a range of 38–44%. The ambient temperature of the room and the material during the experimental study ranged from 20°–24 °C. The top of the chamber was open and all experiments were conducted under the prevailing atmospheric pressure conditions.

Models depicting gas venting in particulate material may be valid for lunar studies because much of the lunar bedrock is covered by a regolith (Schumm, 1970). Coarsely crushed limestone (hereafter referred to as 32–16*,) with 3.5 roundness (Krumbein's classification), mean density of 2.66, apparent sphericity of 0.62, Inman phi mean $(M_\phi)=0.40$, and Trask's sorting coefficient $(So)=0.50$, and finely crushed limestone (60–32* material), roundness 3.5, density of 2.66, 0.73 apparent sphericity, $M_\phi=1.54$, $So=0.86$, were used in this experiment to simulate a possible lunar regolith. The angle of repose for the 32-16 material is 39°, and for the 60-32 material is 41°, and was measured directly from the steepest stable slope on conical heaps formed by pouring the particulate material onto a sheet of paper. The confining geometry of a crater is unlikely to increase these angles much more than the angle of internal friction (ϕ), 43° and 45° respectively for the 32-16 and 60-32 materials as determined by a direct shear test, similar to that used in soil tests. From an analysis of the Apollo 14 transporter-track depths, Mitchell *et al.*, (1972) calculated a range of 40° to 45° for ϕ for the near surface lunar soil.

The 60° slopes exhibited in the 60-32 material after fluidization are anomalous. Not only do the 'fines' adhere to larger particles but also were attracted electrostatically to a plastic measuring ruler. Craters formed using a grounded metal template have

* Refers to the Tyler mesh screen size.

Plate 1. Equipment set-up, showing fluidization chamber, gas pressure and humidity control systems.

angles up to 65°. It is concluded that the electrostatic charges are imposed by the streaming gas in the particulate material and not by the template, and that the steeper slope angle results from electrostatic attraction and/or a 'compaction' and 'cementation' of the material from convecting 'fines' within the bed. The ability of the partic-

ulate material to maintain slope angles greater than the measured angle of internal friction, and the 'true' angle of repose, is termed 'induced cohesiveness'.

It may not be possible to be dimensionally correct in scale models of craters because of the anomalous cohesiveness of very fine materials (Schumm, 1970), and the ballistic and hydrodynamic equations that are important in the formation of large craters and which require scaling to a variable gravitational constant (White, 1971). Nevertheless, natural and experimental phenomena can be studied and correlated by the geometric similitude of the effects to real situations (Pike, 1972). Moreover, the requirement that scaling laws for physical systems be applied only to physically similar systems (White, 1971) is met more readily in fluidization models than in simulated explosion models, in which the strain rate is an important parameter.

The scaling of terrestrial cratering phenomena to lunar conditions apparently is less complicated provided the physical conditions are similar. Size scaling has to be argued on the basis of geometric similitude (Pike, 1972) to terrestrial craters and their origins are linked by analogy. In cratering experiments using chemical explosives in sand under varying gravity and atmospheric conditions Johnson *et al.* (1969) found that for gravities of 0.17, 0.38, and 2.5 times g, the ratio of crater diameters is inversely proportional to the ratios of the gravities to the power n, where n increases to a maximum value of 0.16 at the optimum depth of burial of the explosion. For shallow depths of burst of equivalent energy, the diameter of terrrestial craters should be 0.79 to 0.82 times the diameter of their lunar counterparts. Atmospheric pressure effects likewise are small. The diameters of craters formed at pressures between 1.0 and 5×10^{-4} mm Hg average 1.10 ± 0.02 times those formed under normal (740 mm Hg) atmospheric conditions (Johnson *et al.*, 1969). Their combined effect is a terrestrial to lunar crater diameter scaling ratio of 0.714.

Schumm (1970) noted that fluidization craters blown in a vacuum chamber (8 mm Hg) were morphologically similar but larger than those formed under normal atmospheric pressure conditions. Not only has the effectiveness of fluidization processes been demonstrated at $\frac{1}{6}$ g in a vacuum (Miller and King, 1966), but only $\frac{1}{36}$ th the amount of gas would be required to fluidize an equivalent ash flow on the Moon than on Earth (O'Keefe and Adams, 1965). Apparently terrestrial processes would be enhanced under lunar conditions, and if slope stabilities are similar on both planets, then the geometric similitude arguments of cratering phenomena should be valid. Halajian (1964) reasoned that the angle of repose for cohesionless soils is independent of the gravity field, but for cohesive materials it would be steeper in lower gravity fields, e.g., fine powder with an angle of repose of 52° on Earth could sustain a 90° face on the Moon. On Earth, the angle of repose for most materials is between 30° and 40° (Baldwin, 1963). Lunar slope angles range from $31° \pm 2$ for small craters (Quaide and Oberbeck, 1968) to $41° \pm 3$ for the Straight Wall (Baldwin, 1963). The measured internal friction on loose Apollo 12 soil is 28°, and for dense soil is 34°–36° (Carrier *et al.*, 1972), whereas calculations on the Apollo 14 transporter tracks indicate a range of 40° to 45° for the surface soil (Mitchell *et al.*, 1972). Thus the requirements for similitude appear to be met.

3. Nomenclature, Definitions, and Crater Measurement

Figure 1 and Table I illustrate and list the surface parameters measured in this study. The dimensions of the mean overall crater diameter (D_o), mean crater rim crest diameter (D_r) mean inner flat floor diameter (D_f) and the mean width of the exterior crater rim slope (W_e), were measured directly off the laboratoty crater with a 15 cm ruler. A cross bar and a vertical ruler were used to measure the mean interior relief

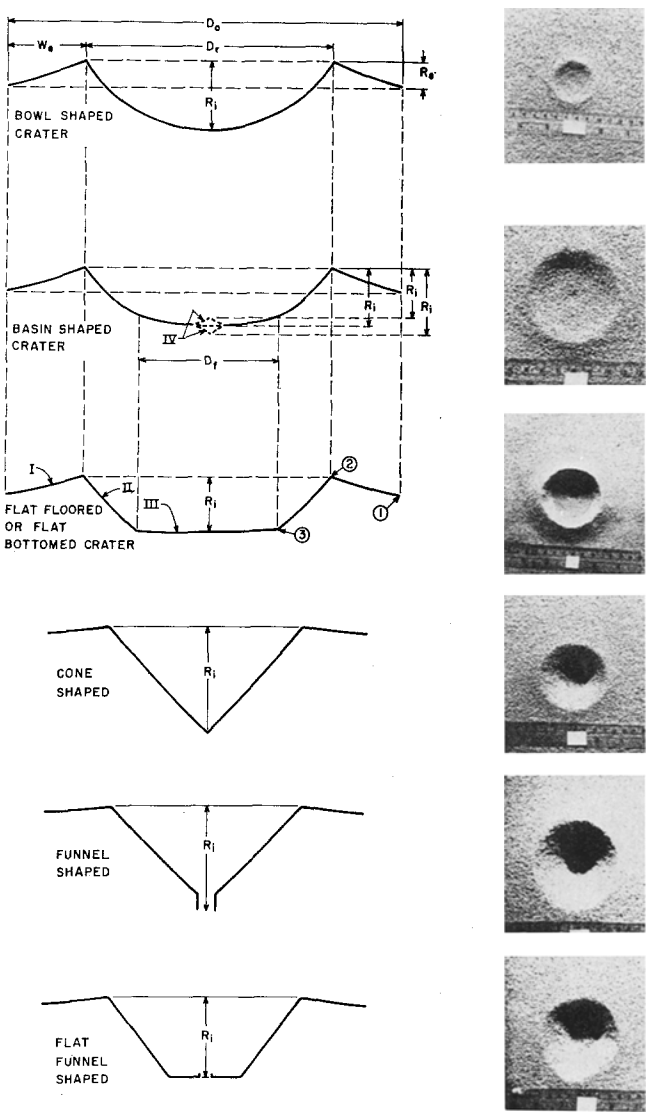

Fig. 1. Cross section sketches (not to scale) and photographs of 6 crater morphologies. Surface dimension notations are after Pike (1968). See Table I for explanation.

TABLE I

Crater nomenclature[a] and parameters

Linear dimensions
D_0 = Mean overall crater diameter
D_r = Mean crater rim crest diameter
D_f = Mean inner flat floor diameter
W_e = Mean width of exterior crater rim slope
R_i = Mean interior relief
R_e = Mean exterior relief of crater rim
Morphologic units
I = Exterior rim slope
II = Interior rim slope
III = Flat interior floor
IV = Central peak or depression
Contacts between morphological units
1 = Foot of exterior rim slope
2 = Crater rim crest
3 = Foot of interior rim slope

[a] After Pike, 1968.

(R_i) and the mean exterior relief of the crater rim (R_e). The exterior and interior rim slopes (I and II, respectively), where amenable, were measured directly with a protractor and ruler to an estimated accuracy of $\pm 2°$. Slopes that could not be measured directly, i.e., between terraces, were calculated from scaled cross-section drawings.

Cross-sections and photographs for the six general types of crater morphologies recognized, are given in Figure 1.

4. Effect of Variables

A. ONSET PRESSURE

The onset of crater development by outgassing is marked by an eruption bubble which preceeds a spouted bed condition and a drop in pressure. The relationship between pressure, y, and thickness, x, for the (60–32) material is linear and denoted by the equation $y=2.89x-3.94$. Additional tests on this material after substantial elutriation and blow over (see graphs A, B and C in Fig. 2) suggest that the onset pressure-thickness relationship changes from a linear to a power function (Figure 2). This is supported by the onset pressure-thickness relationship for the (32-16) material (Figure 3). This effect probably is due to the change in effective density of the gas-small particle phase with progressive elutriation.

Onset pressure can be reduced considerably by tapping or jarring the fluidization chamber. Even though no detailed study was performed, it appeared that the magni-

tude of the pressure drop was proportional to the intensity of the agitation. This effect may be operative on the lunar regolith from the stress generated by lunar tides. This also coincides with the peak 'transient lunar phenomena' activity (Middlehurst, 1967).

B. TIME

A crater obtains a steady-state condition when its parameters are no longer significantly affected by increases in durations of fluidization. Ideally, time lapse photographs of craters should be used to determine the attainment of a steady-state condition. Because of limitations in the photographic system surface parameters were measured directly on 77 craters formed in the (32-16) material and 73 craters in the (60-32) material each with specific durations of fluidization. To insure that each crater was

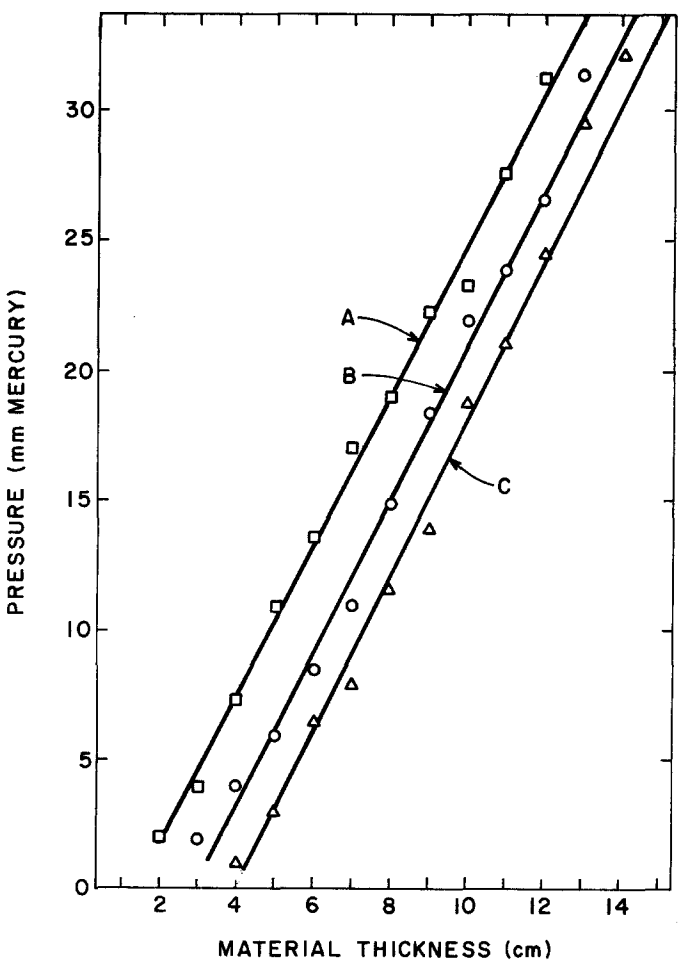

Fig. 2. Minimum pressure necessary for incipient fluidization (spouting). Lines A, B, and C refer to 60-32 material after progressive elutriation. Abscissa for lines B and C are offset respectively one and two units from A.

representative of the appropriate stage of crater development for a continuous gas streaming model, their order of formation was randomized and the rate of pressure application to the fluidization chamber was standardized to minimize initial spouting pressure. Despite the scatter of points in the diagrams most craters were observed to closely follow the growth depicted by the 'best fit' curve.

The dimensions of the width of the exterior slope (W_e), exterior relief of the crater rim (R_e), interior rim slope (II), rim crest diameter (D_r), and mean interior relief (R_i) increase with time as power functions for craters formed in 4 cm of (32-16) limestone at 12.9 mm Hg pressure until steady-states are reached, respectively at approximately, 48, 70, (Figure 4), 70, 100 and 100 s (Figure 5). Whereas the width-depth ratio (D_r/R_i) diminishes with an increase in fluidization duration, the early attainment of

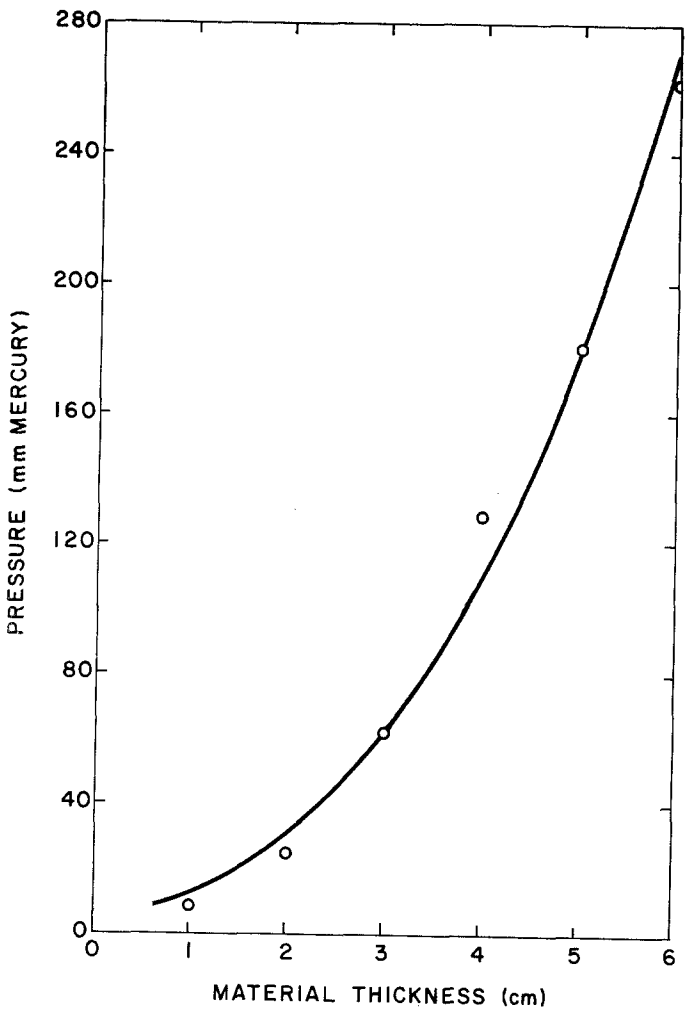

Fig. 3. Minimum pressure necessary for incipient fluidization (spouting) in varying thickness of 32-16 material (not elutriated).

a steady-state condition for rim width and rim height suggests that the dimensions of these parameters are controlled by gas streaming pressures (see subsection 'Pressure').

Interior crater morphology, i.e., bowl or basin shaped, is highly dependent upon the interior rim slope angle (II) which is partly controlled by the apparent cohesion of the particulate material. Because of the importance of ascertaining the genetic difference between bowl and basin shaped and/or flat bottomed craters additional studies were performed on the (32-16) material (Table II). Gas streaming, which progressively causes elutriation and blow over of particulate material and 'fines', changes the mean grain size of the original material. If the concentration of 'fines' in the coarse particulate material from which craters have been developed by gas streaming is relatively high,

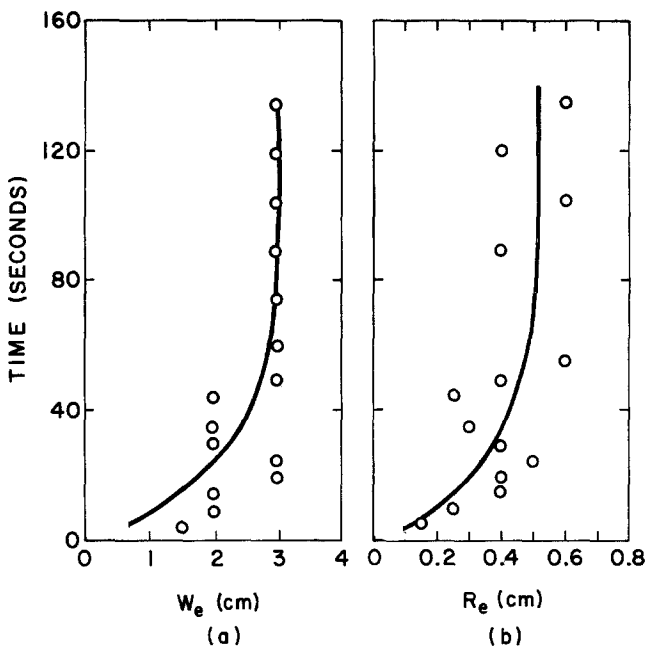

Fig. 4. Relationship between mean width of exterior crater rim slope (a), and mean exterior relief of crater rim (b), with respect to duration of fluidization in 4 cm of 32-16 material at 12.9 mm Hg pressure. Steady states were attained respectively at 48 and 70 s.

the resultant crater will generally be bowl shaped. However, if the amount of 'fines' contained within the particulate material before crater development is near a critical value (dependent upon the grain size distribution, angularity, roundness, and density of the material) the morphology of the crater will depend upon the duration of fluidization. Under these conditions, bowl shaped craters change into basin shaped and/or flat bottomed craters with long durations of fluidization (see Table II). Thus, different crater morphologies either indicate different initial physical characteristics of regolith or changes in conditions caused by different durations of gas streaming. Furthermore, because of the elutriation and blow over effects of gas streaming it may be possible

TABLE II

Variation in morphology with duration of fluidization: elutriation effect in 4 cm of 32-16 material at 12.9 mm Hg

Crater No.	D_r (cm)	R_i (cm)	D_r/R_i	Morphology
Time 30 s				
1	9.1 × 9.6	2.5	3.74	Bowl shaped
2	9.1 × 9.5	2.7	3.44	Bowl shaped
3	8.9 × 9.4	2.6	3.52	Bowl shaped
4	9.0 × 9.6	2.4	3.88	Bowl shaped
5	9.2 × 9.7	2.4	3.94	Bowl shaped
6	8.8 × 9.5	2.3	3.98	Bowl shaped
7	8.5 × 9.2	2.3	3.85	Bowl shaped
8	9.0 × 9.9	2.5	3.78	Bowl shaped
9	9.2 × 9.6	2.5	3.76	Bowl shaped
10	9.3 × 9.5	2.6	3.62	Bowl shaped
Time 60 s				
1	7.5 × 7.7	1.6	4.75	Flat bottomed
2	9.1 × 9.1	2.3	3.95	Bowl shaped
3	9.5 × 9.6	2.8	3.41	Bowl shaped
4	9.0 × 9.5	2.8	3.30	Bowl shaped
5	9.1 × 9.7	2.8	3.46	Basin shaped
6	9.2 × 9.5	2.4	3.90	Basin shaped
7	9.2 × 9.5	2.7	3.46	Basin shaped
8	8.9 × 9.4	2.5	3.66	Basin shaped
9	9.0 × 9.5	2.7	3.43	Basin shaped
10	8.5 × 9.0	2.3	3.80	Basin shaped
Time 120 s				
1	7.5 × 8.2	1.7	4.62	Flat bottomed
2	8.0 × 8.3	1.7	4.79	Flat bottomed
3	8.6 × 9.0	2.4	3.67	Basin shaped
4	9.1 × 9.5	2.6	3.58	Bowl shaped
5	9.0 × 9.4	2.4	3.83	Basin shaped
6	7.5 × 7.0	1.5	4.83	Flat bottomed
7	7.0 × 7.0	1.3	5.30	Flat bottomed
8	8.5 × 8.6	2.3	3.72	Basin shaped
9	9.0 × 9.5	2.4	3.85	Basin shaped
10	7.0 × 7.1	1.3	5.42	Flat bottomed
11	8.5 × 9.0	2.5	3.50	Basin shaped
12	7.5 × 7.5	1.3	5.77	Flat bottomed

to distinguish fresh gas streaming craters from impact craters by the degree of sorting. Gas streaming craters of long durations will be depleted in 'fines' near the central vent area.

To verify the above conclusions for other particulate material sizes, 73 craters were formed in 4 cm of (60-32) material by streaming gas with a pressure differential of 10 mm mercury. The flat bottomed morphology of these craters are unaffected by short durations of fluidization (up to 110 sec), but with long durations of fluidization the stability of the interior crater walls change and cause corresponding variations in the dimensions of overall crater diameter (D_o), rim crest diameter (D_r), inner flat floor

diameter (D_f), and interior relief (R_i). The removal of 'fines' by streaming gas within the crater's interior changes the cohesiveness of the material. For this material, a critical value is reached at 110 s duration of gas streaming as evidenced by the onset of slumping and consequent development of terraces for 19 craters formed with fluidization durations of 110 s and greater (Figure 6). Terraced craters develop from slumping during and after the discontinuation of gas streaming (see 'Discussion'). The crater terraces usually dip at 1 or 2°, multiple terraces are separated by slope angles of 65° (characteristic for this material).

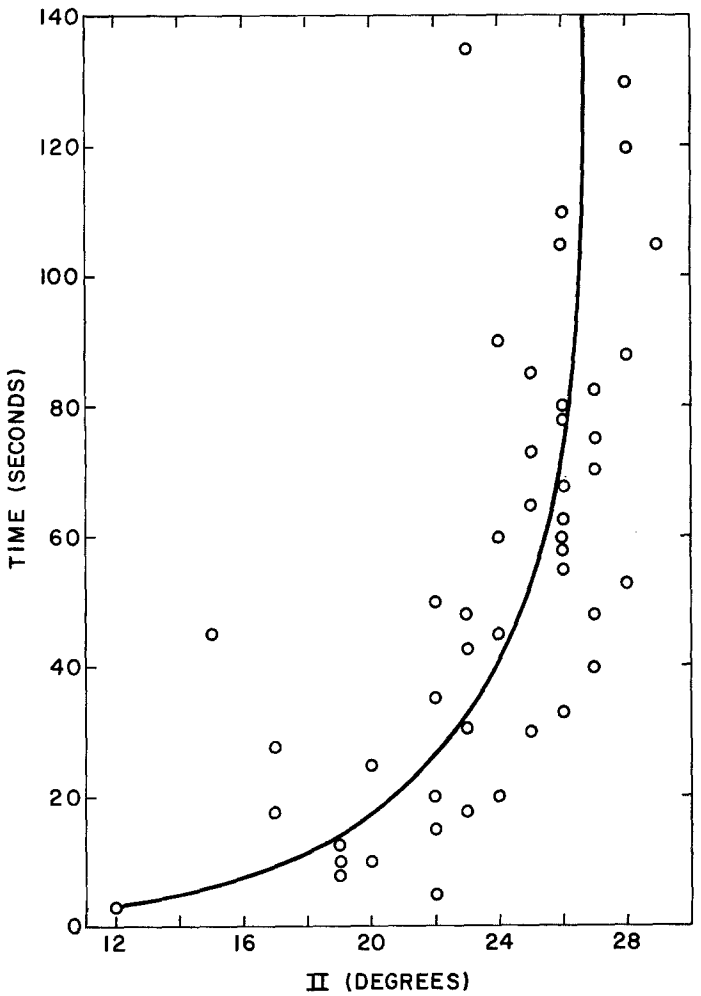

Fig. 5a.

Fig. 5a–c. Relationship between duration of fluidization and (a) interior rim slope, (b) rim crest diameter, (c) interior relief, in 4 cm of 32-16 material at 12.9 mm Hg pressure. Steady states were attained respectively at 70, 100, and 100 seconds. *D_r is the long axis of the horizontal trace of any elliptical craters.

The linear relationship between the rim crest diameter (D_r) and the exterior relief of the crater rim (R_e) (Figure 7) suggest that the rim height of gas streaming craters is not affected significantly by duration of gas streaming but may be controlled by pressure (see subsection 'Pressure' for a complete discussion on this point). These data support the conclusion obtained for crater development in coarse particulate material, that is, the modifications in crater morphologies may indicate only different physical characteristics of regolith caused by different durations of gas streaming and/or different initial properties.

C. PRESSURE

To determine the significance of gas-streaming pressure on the morphology of craters, 4 cm thick (32-16) and (60-32) particulate material was subjected to varying pressures

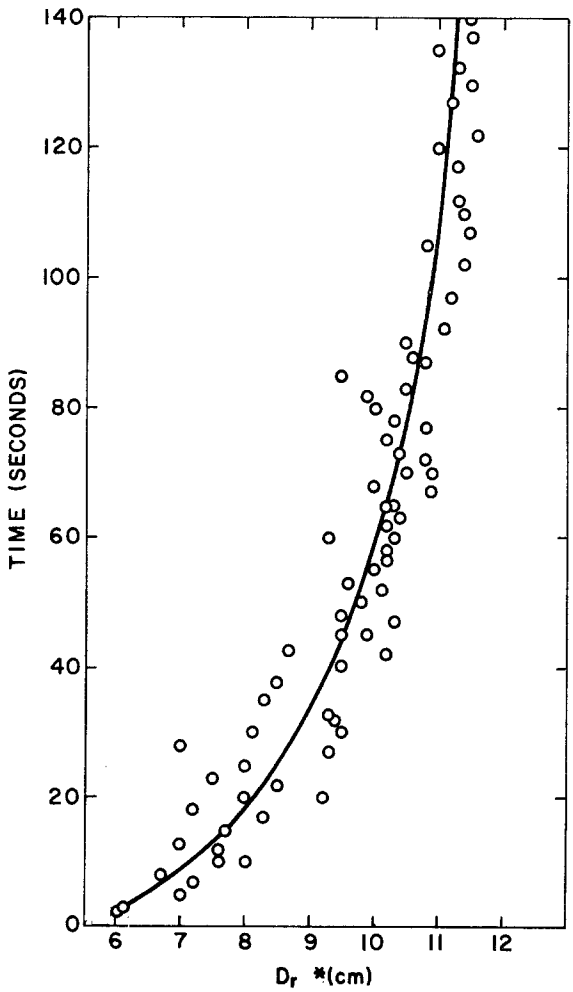

Fig. 5b.

of gas streaming for durations of 150 s. These conditions fulfilled the optimum practical conditions (see subsection, 'Time' and 'Thickness').

With increases in gas streaming pressures (range tested 116 mm Hg to 294 mm Hg) craters formed in 4 cm of (32-16) material undergo morphological transitions from shallow craters with wide flat floors ($D_r = 7.3$ cm, $R_i = 1.4$ cm, $D_f = 5.4$ cm) to deep craters with narrow flat floors ($D_r = 12.2$ cm, $R_i = 4.7$ cm, $D_f = 2.0$ cm). However, the flat bottomed geometry of craters formed in fine material is unaffected by increased gas streaming pressures. Moreover, the 1.5 ratio of the rim crest diameter (D_r) and the inner flat floor (D_f) is unaffected by increases in gas-streaming pressures for all but the first of the 11 craters formed in the 60-32 material. These data are consistent with the conclusion from the previous section.

The interior relief (R_i) of craters formed, respectively, in 32-16 material increase

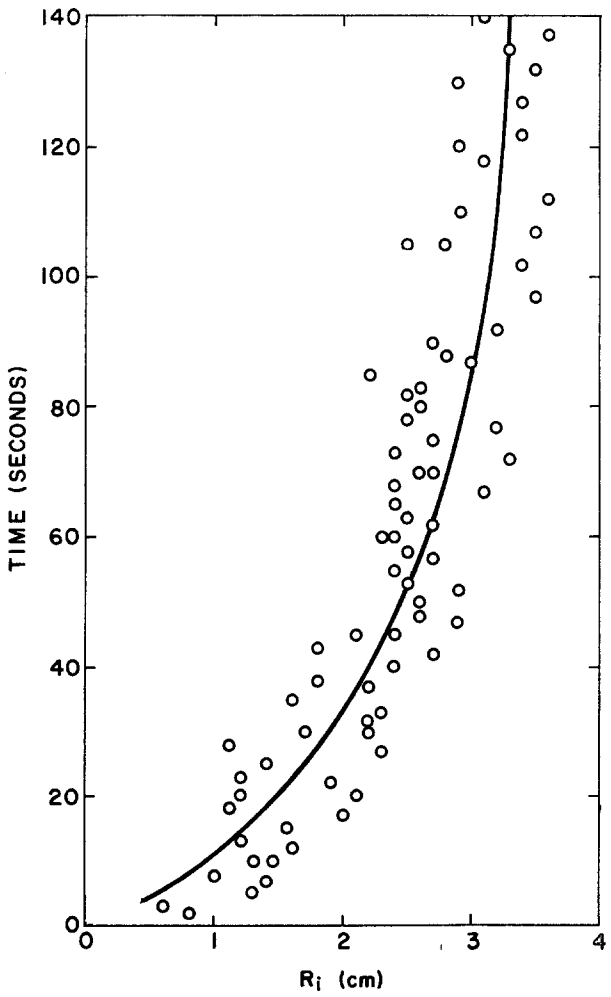

Fig. 5c.

linearly with increasing gas-streaming pressures until the underlying cohesive substrate is encountered (range tested, 1–5 cm thick material). Slight variations in the maximum depth of the craters can exist because depth (R_i) is partly dependent upon rim height (R_e) which varies with pressure (see following paragraphs). Likewise, the diameter of laboratory gas-streaming craters increase linearly with respect to pressure until the maximum depth is obtained; subsequent increases in gas-streaming pressures have no significant effect on the diameter of the resulting crater (Figure 8).

Unlike the relationships between the rim crest diameter (D_r) and the crater depth

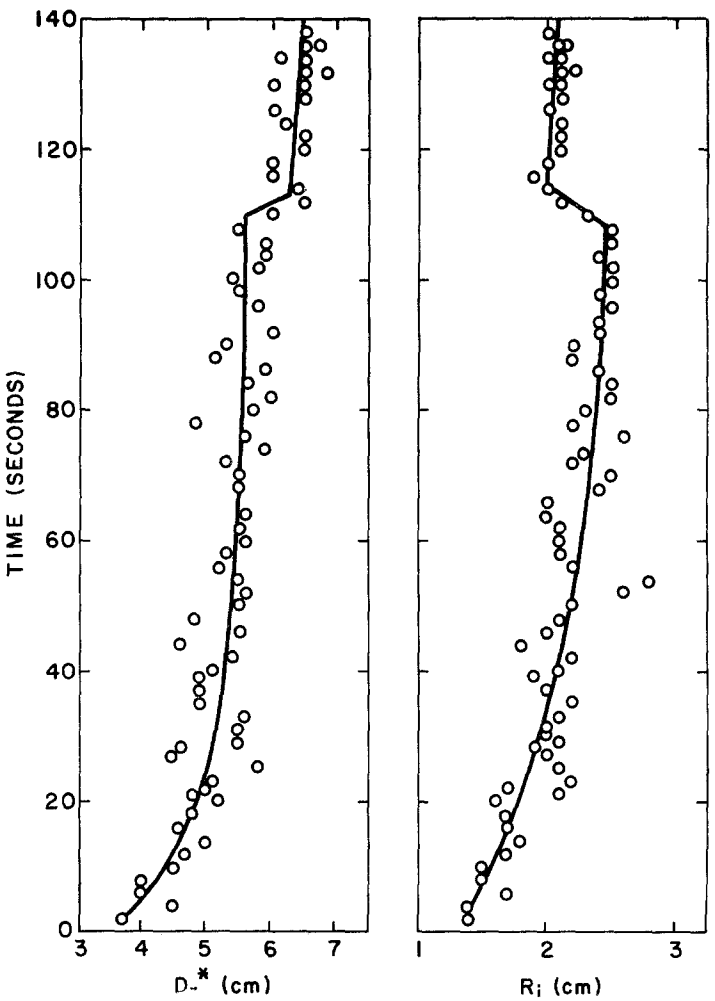

Fig. 6a. Fig. 6b.

Figs. 6a–c. Relationship between duration of fluidization and (a) rim crest diameter, (b) interior relief, and (c) the width/depth ratio, in 4 cm of 60-32 material at 10 mm Hg pressure differential. The break in slope after 110 s defines the critical slumping condition. *D_r is the long axis of the horizontal trace of any elliptical craters.

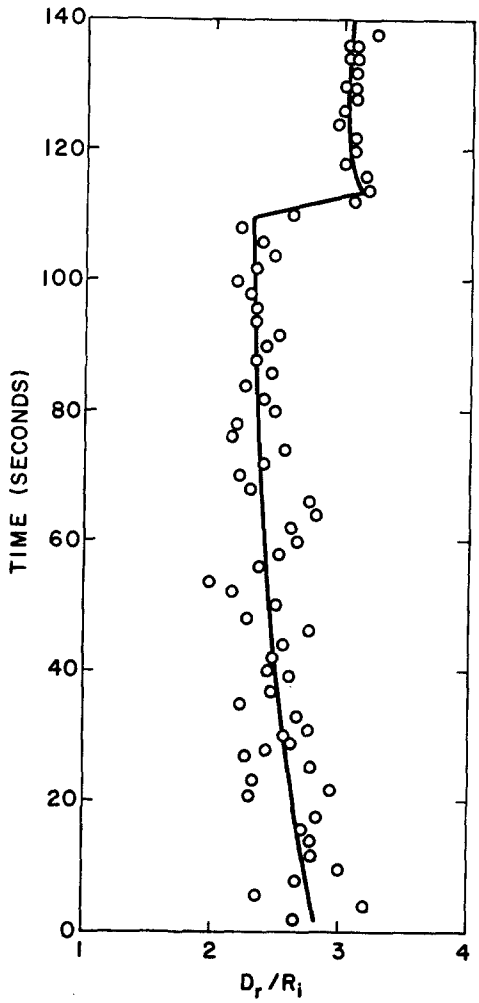

Fig. 6c.

(R_i) for increasing gas-streaming pressures, D_r/R_i is significantly influenced by the physical properties of the material in which the crater forms. D_r/R_i for craters formed in coarse particulate material with depths >3 cm is hyperbolic (Figure 9 and 10) but is unaffected after the initial eruption for craters formed in 60-32 material.

The rims of gas-streaming craters are produced by the initial eruption bubble of the spouted bed condition and the subsequent ejection of material away from the central vent. Ejection distance from the vent depends upon the mass, shape, and trajectory angle of the ejected fragments, in addition to the gas-streaming velocity. Increased gas-streaming pressures on coarse particulate material indicate that the rim height (R_e) of craters increase sympathetically to an optimum value above which ejecta is blown beyond the crater confines (Figure 11). Studies on the 60-32 material support this hypothesis and further suggest that maximum rim development is influenced by the

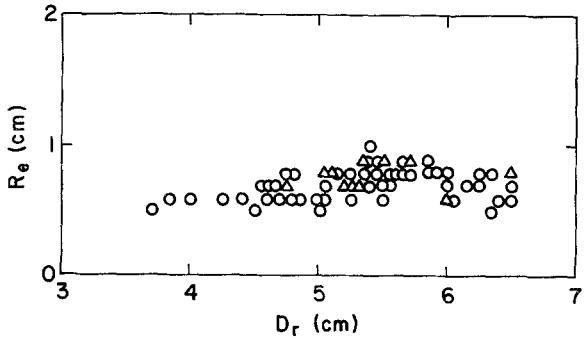

Fig. 7. Relationship between mean rim crest diameter and mean exterior relief of crater rim, in 4 cm of 60-32 material at 10 mm Hg pressure differential. Δ's indicate points from duplicate runs.

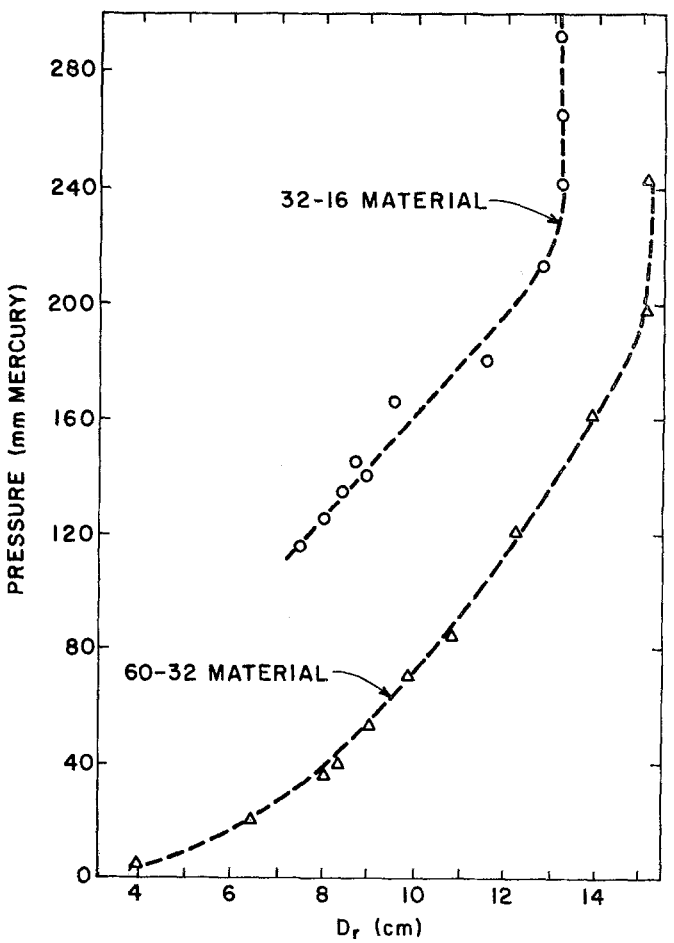

Fig. 8. Relationship between mean crater rim crest diameter and pressure, in 4 cm thick materials for 150 s duration of fluidization. Note how the crater diameter remains constant above the critical pressure of 200 and 240 mm Hg respectively for the 60-32 and 32-16 materials.

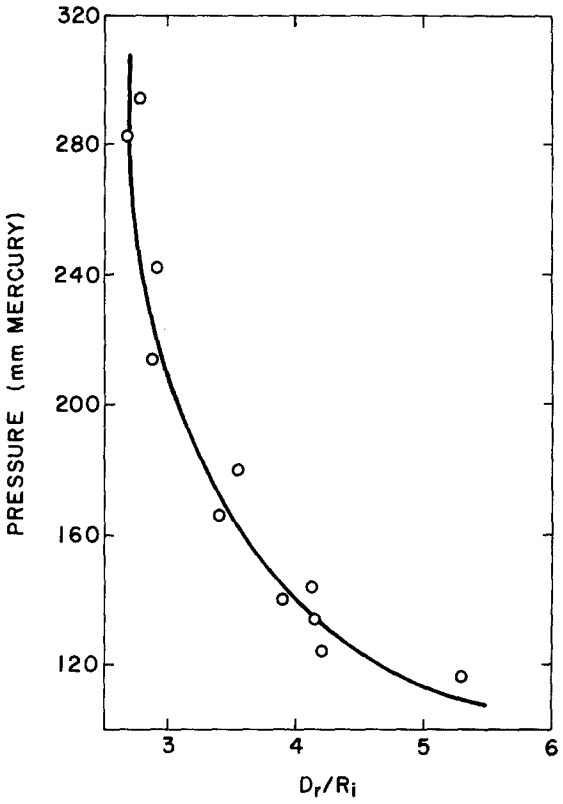

Fig. 9. Hyperbolic relationship of the mean rim crest diameter – mean interior relief, with respect to pressure, in 4 cm of 32-16 material for 150 seconds duration of fluidization.

angle of repose and the gas-streaming pressures required to initiate spouting for different grain size fractions. Thus, a maximum value of rim height (R_e) is obtained when the gas streaming pressure is sufficient to remove all of the material from the vent area and deposit it within close proximity of the crater. If the gas-streaming pressure is too great the particulate material is blown away from the crater resulting in an essentially rimless crater. Accordingly, rim width (W_e) increases with a pressure increase.

D. REGOLITH THICKNESS

Because of the importance of linking crater morphology to varying regolith depth, three different series of experiments were performed on varying thicknesses of coarse (32-16) material.

In the first, gas was blown through various thicknesses of coarse limestone at gas streaming pressures with constant differentials of 10 mm Hg above the mean incipient fluidization value for specific material thicknesses (Table IIIa). No significant variation exists in the morphology or dimensions of craters formed within specific regolith

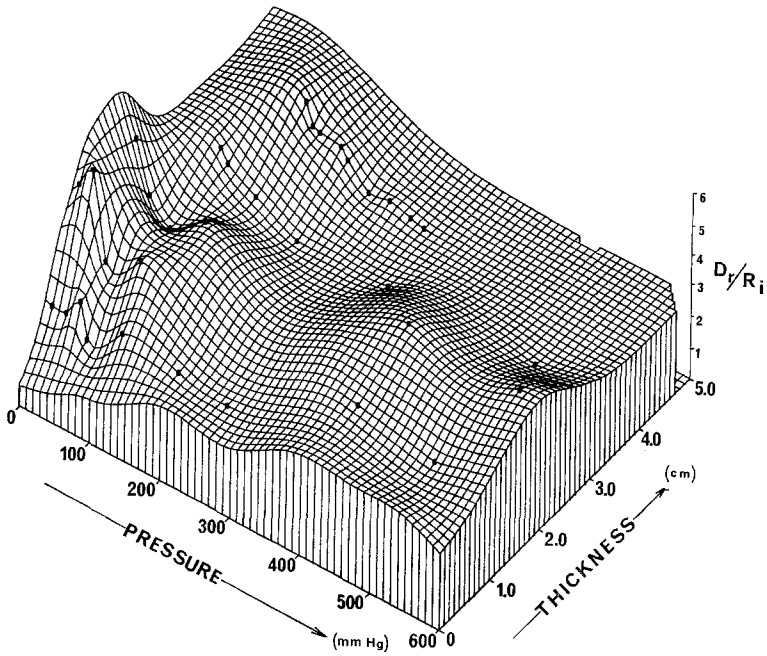

Fig. 10. Axonometric projection (pressure in mm Hg, thickness in cm, D_r/R_i) for 'critical thickness' of crater development in 32-16 material. In thicker regolith (>3 cm) the D_r/R_i ratio decreases hyperbolically with increasing pressure. D_r/R_i for craters in thinner regolith (>3 cm) are less predictable because of substrate effects and because minor fluctuations in accuracy are amplified in the crater parameters measured.

thicknesses (5 were formed in 1 cm, 2 cm, 3 cm thick material; 3 in 4 cm; 2 in 5 cm). With increasing regolith thickness and constant gas streaming differentials (for uniform durations of fluidization) craters undergo changes in morphology from basin (1 cm thick material) to bowl (2 cm) to funnel (4 cm) to unstable cones (>5 cm) which decay into bowl or basin shaped craters.

In the second, an attempt was made to minimize variability in crater development which may have resulted from fluctuations of incipient fluidization pressure for specific fragmental thicknesses. A series of craters were blown in which an additional pressure of 10 mm Hg was applied to each crater after the onset of the incipient fluidization stage. The results (Table IIIb) were similar to the first experiments and suggests that for this material and pressure differential of 10 mm Hg an optimum thickness of 4 cm produced cone and/or funnel shaped craters. The low cohesive properties of this material are incapable of maintaining the cone and/or funnel shape crater morphology (for thicknesses greater than 4 cm) after cessation of gas flow. Slumping of material from the interior crater walls to the center of the crater occurs changing its cone and/or funnel shaped morphology to a bowl or basin shaped one.

Graphically, an inflection occurs for the linear increase of the rim crest diameter (D_r) at 4 cm (Figure 12) which coincides with the onset of slumping within the crater. There is a corresponding levelling out of the crater depth curve.

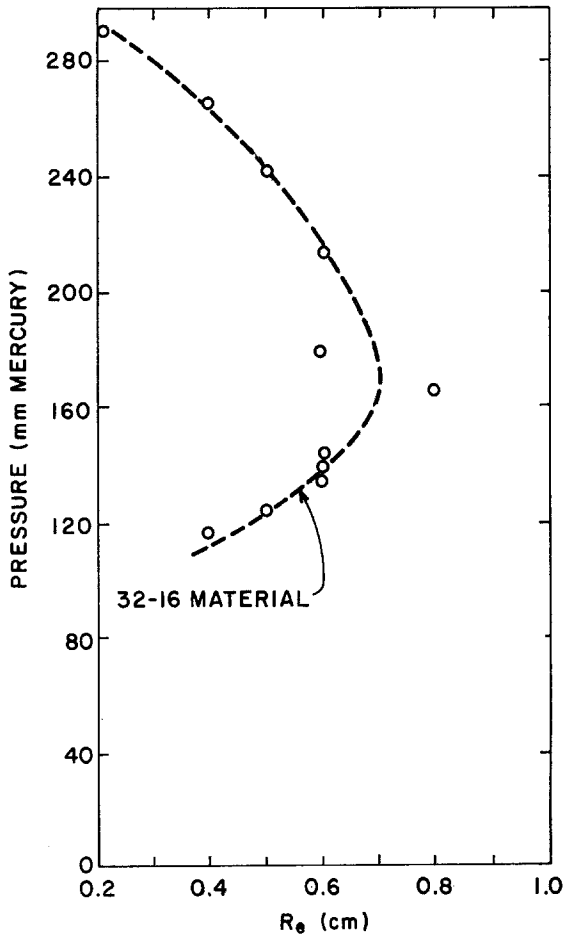

Fig. 11. Parabolic relationship between mean exterior relief of crater rim and pressure in 4 cm of 32-16 material for 150 seconds duration of fluidization. Pressures greater than 170 mm Hg were sufficient to blow ejecta well beyond the crater confines. The exterior relief of these craters should be low and relatively uniform.

The agreement of these data with those on Table III leads us to conclude that the cohesiveness of the material during and after gas streaming is critical in determining the morphology of the resulting crater. However, the importance of gas-streaming pressure as a determining factor on the crater morphology cannot be overlooked. With high gas-streaming pressures the funnel and cone shaped morphology is capable of being maintained after cessation of gas flow in thicker regoliths (refer to the following paragraphs).

The final series of experiments were performed to determine the effect of increasing regolith thickness with constant values of gas-streaming pressure (depicted in Plate 2).

For pressures of 192 and 240 mm Hg, craters undergo a transition in morphology from funnel (Plate 2a, in 1 cm thick material), to flat funnel (Plate 2b, c, d, e, of respectively 2, 3, 4, and 5 cm thick), to basin shaped (Plate 2f, 6–8 cm thick). The

TABLE III

Crater parameters in varying thickness of 32-16 material, fluidized for 150 s at different differential pressure. In (a) average pressure differential values are given for several craters measured; in (b) they represent only one crater

(a) Variability in crater dimensions at 10 mm Hg above the mean incipient fluidization values

Crater No.	D_r (cm)	R_i (cm)	R_e (cm)	W_e (cm)	I (deg)	II (deg)	Morphology
1 cm Thick at 12 mm Hg Pressure							
1	2.6 × 2.9	1.0	0.1	1.0	–	55	Basin shaped
2	2.8 × 3.0	0.9	0.2	1.2	2	55	Basin shaped
3	3.3 × 3.4	1.2	0.3	1.3	4	55	Basin shaped
4	2.9 × 3.2	1.1	0.3	1.2	4	55	Basin shaped
5	3.0 × 3.1	1.0	0.2	1.3	4	55	Basin shaped
2 cm Thick at 21 mm Hg Pressure							
1	5.0 × 5.2	1.7	0.4	1.8	4	52	Bowl shaped
2	5.0 × 5.1	1.7	0.4	1.8	4	53	Bowl shaped
3	5.1 × 5.1	1.7	0.4	1.8	4	51	Bowl shaped
4	5.0 × 5.0	1.7	0.4	1.7	3	52	Bowl shaped
5	5.1 × 5.2	1.7	0.4	1.8	4	51	Bowl shaped
3 cm Thick at 40 mm Hg Pressure							
1	6.8 × 6.9	3.3	0.4	3.0	6	56	Cone shaped
2	7.0 × 7.2	2.7	0.3	3.1	6	52	Basin shaped
3	6.1 × 6.5	2.2	0.3	3.0	5	53	Basin shaped
4	7.0 × 7.1	2.8	0.3	3.1	6	54	Basin shaped
5	6.5 × 6.7	2.9	0.5	3.1	6	52	Basin shaped
4 cm Thick at 120 mm Hg Pressure							
1	8.5 × 9.3	4.3	0.6	4.0	7	58	Funnel shaped
2	8.2 × 9.2	4.2	0.6	4.0	7	58	Funnel shaped
3	8.4 × 9.1	4.2	0.6	4.0	6	58	Funnel shaped
5 cm Thick at 140 mm Hg Pressure							
1	9.0 × 9.5	–	–	–	–	–	Cone (very unstable)-decay to bowl and basin.
2	9.1 × 9.4	4.4	–	–	–	–	Cone (very unstable)

(b) Single crater dimension for 10 mm Hg above the onset of incipient fluidization

Thickness	D_r	R_i	R_e	W_e	II	Morphology
1 cm	4.0 × 4.1	1.3	0.3	1.5	45	Bowl shaped
2 cm	6.5 × 6.5	2.1	0.4	2.0	50	Bowl shaped
3 cm	8.6 × 8.7	2.8	0.5	3.0	50	Bowl shaped
4 cm	11.0 × 11.5	4.6	0.6	5.5	45	Cone shaped
5 cm	11.5 × 12.5	4.5	0.7	4.0	50	Bowl shaped
6 cm	12.6 × 12.8	4.5	0.7	4.0	55	Flat funnel to bowl
7 cm	13.0 × 14.2	5.1	0.7	4.0	55	Funnel to bowl

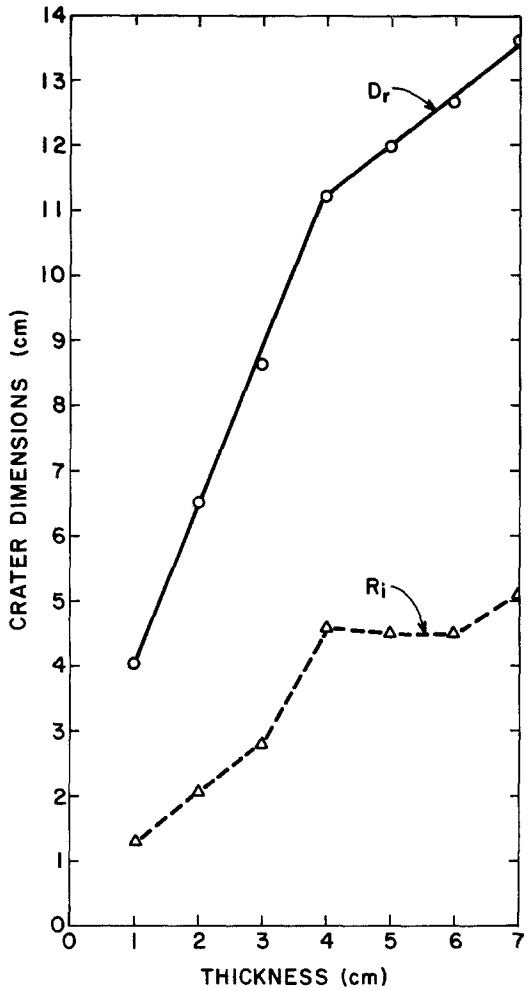

Fig. 12. Relationship between mean crater rim crest diameter and mean interior relief respectively, with respect to thickness in 32-16 material, at constant pressure of 10 mm Hg above the incipient fluidization pressure. The break in both curves at 4 cm depth of 'regolith' reflects the development of slumping conditions in the craters.

deflection in the (D_r) curves coincides with a change in crater morphology from funnel, to flat funnel and bowl, and also separates Schumm's (1970) 'explosion' from 'fluidization' craters. It represents the critical thickness of material necessary for the fluidization process to progress beyond the eruptive bubble stage. Whereas the crater diameter increases with increasing regolith thickness, crater depths decrease and become uniform (Figure 13) after reaching a critical value that coincides with the onset of slumping. These data are in general agreement with the experimental work of Schumm (1970), who determined the morphology of the resulting features when varying thicknesses of sand and marble dust were fluidized from vents of various sizes and configurations.

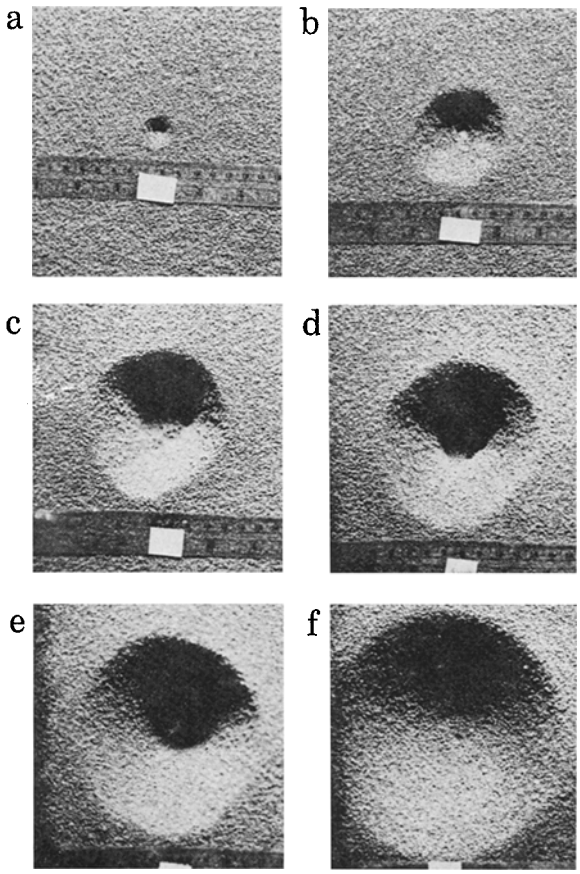

Plate 2. Craters developed in increasing thicknesses of 32-16 material at 192 mm Hg pressure after 150 seconds. Regolith depths are respectively (a) 1 cm, (b) 2 cm, (c) 3 cm, (d) 4 cm, (e) 5 cm, (f) 6 cm.

It was noted that jarring the chamber induced eruption and spouting at lower than normal pressure (see Figure 13 for inflection of the (D_r) curve at 6 cm 'regolith' thickness for 192 mm Hg pressure). Lateral accelerations evidently promote channelling and premature eruption (see section on 'Onset Pressure'), and such vibrations may be natural in real situations.

5. Discussion

A. TERRACE DEVELOPMENT

Terraces in craters have been interpreted either as substrates of different competency or as slump features. In our experiments terraced craters (see Plate 3) were produced by slumping during the fluidization process and/or relaxation of the fluidized bed after the cessation of gas flow.

The requirements for terrace formation are:

(a) that the host material have cohesive properties that increase as a result of an

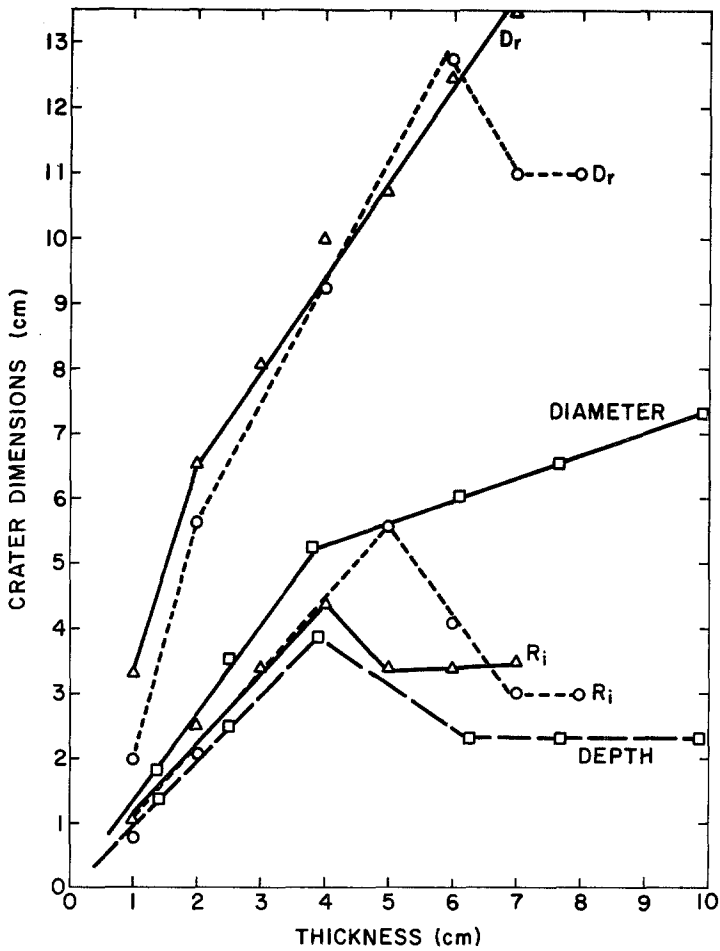

Fig. 13. Composite diagram showing variation in the mean crater rim crest diameter, the mean interior relief, with respect to 'regolith' thickness at constant pressure. The deflection in the diameter curves coincides with a change in crater morphology from funnel, to flat funnel and basin, and corresponds respectively to Schumm's (1970) 'explosion' vs 'fluidization' craters. The deviation in the D_r–192 mm Hg curve at 6 cm 'regolith' thickness is due to jarring of the fluidization chamber. ○'s – 192 mm Hg, 32-16 material; △'s – 240 mm Hg, 32-16 material; □'s – Schumm's data (Schumm, 1970).

applied electrostatic charge from the streaming gas and/or by 'cementation' or 'compaction' by convecting 'fines';

(b) that the material be sufficiently cohesive to support the additional rim load and produce discrete slump terraces after failure. The greater the shearing strength of the material the more pronounced the terrace development, and the greater the likelihood of producing a central mound in the crater floor;

(c) that the outgassing pressure be more than 2 but not more than 20 times the incipient spouting pressure. These pressures are sufficient to remove the fragmental

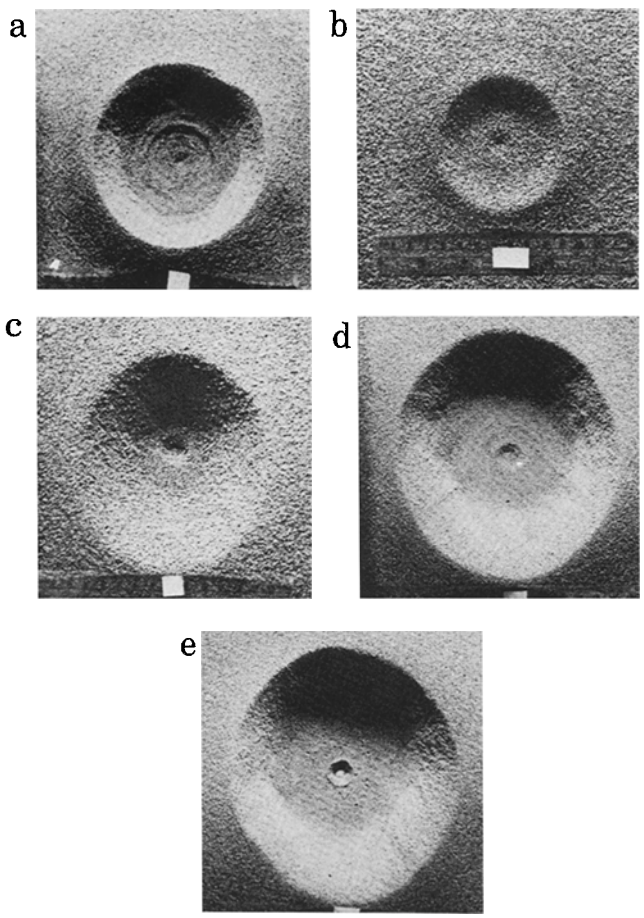

Plate 3. Some central depression and terraced craters developed in a fluidized bed 4 cm thick after 150 s. (a) Terraced crater in 60-32 material and 85 mm Hg pressure. (b) Central depression crater with wide floor in 32-16 material and 124 mm Hg pressure. (c) Central depression crater with narrow flat floor in 32-16 material and 294 mm Hg pressure. (d) Flat-floored central depression crater with craterlets in 60-32 material and 200 mm Hg pressure. (e) Flat-floored central depression crater with craterlets in 60-32 material and 245 mm Hg pressure.

material from the vent area and deposit it on the exterior rim slope but not blow it completely beyond the crater confines.

Multiple outgassing events of different magnitudes could either enhance or destroy pre-existing terraces.

B. CENTRAL DEPRESSION CRATERS

The origin of central depressions in some craters has been interpreted as (a) impact generated, reflecting the presence of an underlying cohesive substrate (Quaide and Oberbeck, 1968), (b) as the vent of a diatreme or blow hole (Cameron and Coyle, 1971). Outgassing craters with central vents (see Plate 3) formed independent of material and

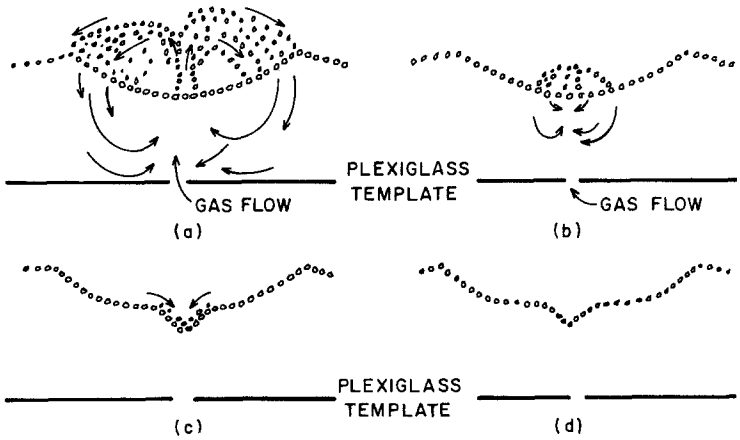

Fig. 14. Schematic cross sections of a fluidized bed, illustrating the development of a central depression in a broad, flat-floored crater, at low fluidization pressure. Note that most of the ejecta fall within the crater confines, and that the central vent is formed by the emission of entrained gas.

thickness at (a) low fluidization pressures by recycling particulate material within the crater confines and subsequent collapse over the vent area with emission of the entrained gas (see Figures 14a–d) and (b) at high fluidization pressures by slumping during the terminal stages of outgassing and subsequent collapse over the vent area in the coarse particulate material (32-16) (see Figures 15a–c). However, in the more cohesive material (60-32) the vent formed during defluidization of the moving bed is a process similar to that depicted in Figures 14a–d.

In uncontrolled experiments in finely granulated sugar craters with central mounds

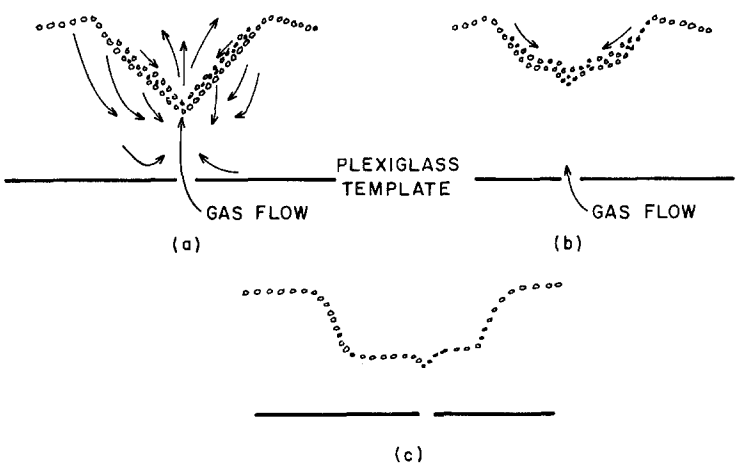

Fig. 15. Schematic cross sections of a fluidized bed, illustrating the development of a central depression in flat funnel crater, at high fluidization pressures. Slumping is active, and the central depression is caused by collapse of the vent.

formed independent of thickness, as a result of slumping during the terminal stages of fluidization.

C. CRATERLETS

In the floor of some large craters, craterlets were observed (see Plates 3d and e). While some are formed by fall back material (impact), others are due to channeling, and by collapse into subjacent voids with cessation of gas flow.

D. REGOLITH THICKNESS

Even though most selenologists agree that the lunar regolith is composed of both volcanic flows and pyroclastic materials, and the fragmental products of impact comminution, there is no agreement for its depth. On the assumption that the observable small lunar crater population is impact generated Oberbeck and Quaide (1967, 1968) and Quaide and Oberbeck (1968) conclude that 'normal geometry' craters have an apparent rim crest diameter to regolith depth ratio less than 4.2 (variation in the position of the boundary separating 'normal' from 'flat-bottomed geometry' is from 3.8–4.2) and 'concentric geometry' craters have ratio values greater than 10 (range of variation between 'flat-bottomed' and 'concentric' craters is from 8–10), 'flat-bottomed' craters have intermediate ratios.

High resolution Orbiter photographs reveal many areas where small fresh normal, flat bottomed, and concentric craters are in close proximity. By use of these criteria on site P12 b2 (see Plate 4 of High Resolution Orbiter III-182 H) in Oceanus Procellarum, the concentric craters (d, e, and f) indicate, respectively, regolith thickness of approximately 8.5, 14, and 8 m, whereas the normal craters (a and c) indicate regolith thicknesses greater than 63 and 51 m, respectively. The regolith at flat bottomed crater (b) should be between 25 and 60 m thick. Based solely on the impact model this would necessitate a regolith of varying thickness and steep gradients beneath the relatively flat mare surfaces, an interpretation that has also been questioned by Cameron and Coyle (1971).

Cameron and Coyle (1971) suggest a correlation between boulder distribution, crater morphology and origin. Widespread distribution of boulders in concentric craters are thought to be impact in origin, whereas, relatively deep broad rimmed craters containing boulders only within and on their ramparts are of endogenic origin. Shallow rimless craters with no apparent boulders could be degraded forms of either. Our experiments clearly demonstrate that normal (bowl), flat bottomed and basin shaped, and funnel shaped craters can be formed by streaming gas. Furthermore, they can form in various depths of fragmental material. Although Emmons (1965) and Mills (1969) generated 'concentric' craters by fluidization, ours (see Plate 3a) are not as well developed as theirs.

Our experiments suggest that funnel, flat funnel and, perhaps, cone-shaped craters having boulders within and on their ramparts may indicate regolith depth. High gas-streaming pressures have the ability to blow material (boulders) well beyond the rim and form essentially rimless craters. If the pressures are just great enough to clear the

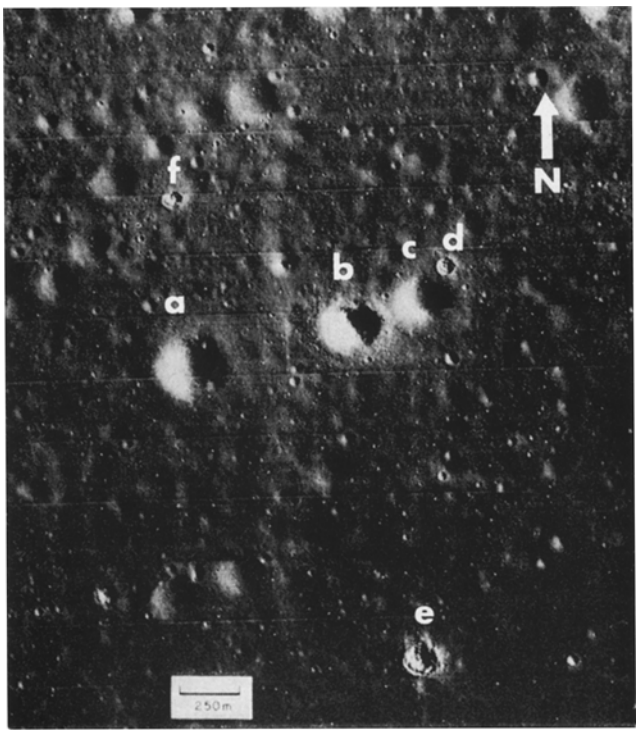

Plate 4. High-resolution Orbiter III photograph, No. 182 H_1 of part of Oceanus Procellarum. Note concentric craters (d, e, and f) in close proximity to normal craters (a and c). Crater (b) has a flat floor.

vent area of overlying fragmental material, but not eject the material outside the confines of the crater, the cohesion of the material has to be sufficiently high to prevent slumping and thus transforming them into bowl or basin shaped craters. Craters formed in deep 'regolith' irrespective of pressure will probably be bowl or basin shaped (see Table III). Some of the constraints are that the gas pressure should exceed the horizontal stress plus the average tensile strength of the superincumbent rocks and that the magma should crystallize at depth, i.e., should not well up into and destroy the vent. Magmas of high volatile content (H_2O and/or CO_2) become oversaturated in volatiles as they rise and exsolve a separate fluid (gas) phase (Harris *et al.*, 1970). Supersaturation and exsolution results in an increase in volume, which in the case of crystallization and boiling at 500 bar can be as much as 53% (Burnham, 1972). The mechanical energy released during crystallization and outgassing of a magma initially containing 2.8 weight percent water in the pressure range of 400–1700 *b* is greater (Burnham, 1972) than the average kinetic energy of approximately 2.6×10^{23} erg km^{-3} of magma in explosive volcanic eruptions (Yokoyama, 1957), and this neglects the potential energy of raising the magma and kinetic energy of adiabatic expansion of the volatiles to the ambient atmospheric pressure at the surface. The work done in

adiabatic expansion can be considerable, e.g., 0.5% volatiles (mainly H_2O) in a magma exsolving at 60 km depth would yield approximately 10^{24} erg km^{-3} magma. However, much of this would be used in drilling, comminution, and transportation. Thus sufficient energy (see Baldwin, 1963 for estimates) to produce Meteor Crater (1.2 km diameter and 10^{22}–10^{23} erg) or even New Quebec Crater (3.2 km diameter and 10^{24}–10^{25} erg) are available from magmatic sources of appropriate volatile content if the mechanical energy can be released explosively at the surface.

The higher the volatile content, the greater the depth of outgassing and solidification of the magma and consequent development of a solid-gas fluidization system such as are thought to be responsible for the formation of diatremes. Pipes would form at fracture intersections or under conditions of nearly equal horizontal stress, while unequal horizontal stresses would favor the formation of dikes and fissures. Estimates of initial water content of magmas range from up to 20% plus for kimberlitic, 0.4–15% for basaltic, and 6–8% for granitic types (Harris *et al.*, 1970). Despite the apparent dryness of lunar rocks, 150-455 ppm H_2O in breccias and 810 ppm in soil 'fines' (Mason and Melson, 1970), they should produce some volatiles during crystallization. In addition cratering processes would be more efficient in a thick regolith.

E. TERRESTRIAL ANALOGIES

The presence of lapilli, rounded fragments, extreme stratigraphic mixing of inclusions, and the lack of appreciable thermal and dynamic metamorphism in kimberlite and carbonatite pipes, and certain diatremes of great vertical extent, suggest a non violent emplacement mechanism. The pipes generally are small, funnel shaped, and tend to occur in clusters. These features have led many investigators (Harvie, 1910; Osborne and Grimes Graeme, 1936; Reynolds, 1954; Dawson, 1962, 1967; Gold and Marchand, 1969; McGetchin, 1968, 1970) to suggest a gas streaming or fluidization mechanism for their origin. Other volcanic features, such as the explosion craters in Basotu, Tanzania (Downie and Wilkinson, 1962) and the flat floored ring-craters (maars up to 8 km across) near Ruvenzori, Uganda (Holmes, 1965) are considered to be fluidization craters. Not only are the latter amongst the largest known fluidization craters but they also have a circularity that overlaps in degree with the impact craters (Murray and Guest, 1970). Perhaps their occurrence in the thick (several kilometers), semi-consolidated sediments in the rift valley floor is significant.

Gas streaming velocities in excess of 450 m s^{-1} have been calculated (McGetchin, 1970) using numerical solutions for idealized steady gas flow in diatremes from the expansion of a volatile phase in a reservoir (volatile rich concentrations at 100 km depth) to the Earth's surface, whereas, the adiabatic expansion of the streaming gas could reduce gas temperatures to −53 °C (McGetchin, 1970). A vent pressure of 540 bar and a minimum muzzle velocity of 191 m s^{-1} are indicated for the Hole in the Ground Maar, Oregon (Lorenz *et al.*, 1970). Not only is a gaseous source available in regions of intrusive activity, but the outgassing fluids also appear to have sufficient energy to erode vents in bed-rock and fluidize low cohesion surficial materials to form craters.

The departure of the surface trace of endogenic craters from a circle is greater than for meteorite and artificial explosion craters, and various circularity indices have been used (Murray and Guest, 1970) to discriminate them. Even though most of the experimental fluidization craters are slightly elliptical in plan (see Plates 2 and 3; Tables II and III), all have a circularity index within the latter group. The elliptical nature of these craters are influenced by the rectangular configuration of the fluidization box (wall effects), and the direction of spreading of the particulate material (fabric).

6. Conclusions

(1) Craters of different morphology can be formed in particulate material by gas streaming. The morphology of fluidization craters is dependent upon the physical properties of the host material, the gas pressure, the 'regolith' depth, and the duration of gas streaming. If the regolith is sufficiently thick for the fluidized bed to be free from bedrock configuration control (joints, etc.), and relatively free from horizontal physical gradients (positional and orientational fabric), then the resulting crater(s) should have a polar axial symmetry and high circularity, and they will be similar in morphology to impact craters.

(2) Cone, funnel, and flat funnel shaped craters are indicative of high gas streaming pressures in relatively thin regolith. In thicker regolith or low cohesion materials, slumping associated with the terminal phase of fluidization modifies them into bowl, basin, and central peak craters.

(3) Terraces within craters develop by slumping during the waning stages of fluidization, and they form regardless of regolith depth and depend mainly on cohesion and outgassing pressure.

(4) Central depression craters develop from the collapse of the fluidized bed over the vent, and form independent of the material or regolith thickness.

(5) Craterlets (some funnel shaped) are formed by impacting ejecta fragments and by the collapse of secondary channels.

(6) With prolonged gas streaming (a) the width/depth of fluidization craters decreases and is sensitive to any reduction in cohesiveness of the material, and (b) the finer fragments are selectively blown out of the crater.

(7) The inner crater wall slope may be up to 20° steeper than the unconfined angle of repose for the material and reflects increased cohesiveness due to electrostatic charges induced by the streaming gas, and/or a 'compaction' and 'cementation' of the material from convecting 'fines' within the bed, and by the confining geometry of the crater floor in loading the 'toe' of potential land slides.

(8) In the fluidization model, any boulders within the crater are more likely to be observed after it has undergone prolonged gas streaming.

(9) Only if the crater producing process is known can crater morphology be used to give limits of regolith depth.

(10) Because of the anomalously high number of small lunar craters (<2.8 km across) and the possibility of active outgassing of lunar magmas (vesicular lunar rocks,

transient lunar phenomena, and periodic presence of water vapor) through a thick regolith, we conclude that many of the smaller lunar craters could have been formed by endogenic fluidization processes.

Acknowledgements

We gratefully acknowledge support of this work under NASA Grant NGL 39-009-010. We also acknowledge the help of Dr Peter Deines in the design of the fluidization chamber, the photographic technical assistance of Mr J. Moore, and the discussions with Drs F.-E. Wickman, S. Alexander, and F. Dachille. We thank NASA for the use of Orbiter III photograph #182 H, and Mr E. Gelinas and Dr J. Popelář of the Earth Physics Branch, Department of Energy, Mines and Resources, Ottawa, respectively, for preparing some of the photographs and the axonometric diagram.

References

Baldwin, R.: 1963, *The Measure of the Moon*, University of Chicago Press, Illinois, p. 488.
Burnham, C. W.: 1972, *Earth Mineral Sci. Bull.* **41**, 69.
Cameron, W. S. and Coyle, G. J.: 1972, *The Moon* **3**, 159.
Carrier, W. D. III, Bromwell, L. G., and Martin, R. T.: 1972, *Third Lunar Sci. Conf.*, Lunar Science Inst., Houston, p. 119–121.
Davis, J. R. and Rohlfs, D. C., 1964: *J. Geophys. Res.* **69**, 3257.
Dawson, J. B.: 1962, *Geol. Soc. Amer. Bull.* **73**, 545.
Dawson, J. B.: 1967, in P. J. Wyllie (ed.), *Ultra-Mafic and Related Rocks*, John Wiley and Son, N.Y., p. 241.
Downie, C. and Wilkinson, P.: 1962, *Bull. Volcanologique* **24**, 389.
Emmons, R. C.: 1965, *Tectonophysics* **2**, 83–89.
Fielder, G.: 1965, *Lunar Geology*, Lutterworth Press, Great Britain.
Freeman, J. W., Jr., Hills, H. K., and Vondrak, R. R.: 1972a, 'Water Vapor, Whence Comest Thou?', *Lunar Sci. Inst. Contrib.* No. 88, Revised Abstracts of Papers Presented at the Third Lunar Science Conference, p. 283–285.
Freeman, J. W., Jr., Hills, H. K., and Vondrak, R. R.: 1972b, $E \oplus S$ **53**, 439.
Gold, D. P. and Marchand, M.: 1969, in G. Pouliot (ed.), *Geology of the Monteregian Hills*, Geol. Assoc. Canada: Mineralogical Assoc. Canada Guidebook, p. 5–42.
Green, J.: 1965, in H. Whipple (ed.), *Geological Problems in Lunar Research, Annals N.Y. Acad. Sci.* **123**, 403.
Halajian, J. D.: 1964, in *Lunar Surface Material Conference, Boston, 1963, Lunar Surface Layer; Materials and Characteristics*, Academic Press, N.Y., p. 67–91.
Harris, P. G., Kennedy, W. Q., and Scarfe, C. M.: 1970, in G. Newall and N. Rast (eds.), *Mechanism of Igneous Intrusion, Liverpool Geol. Soc. Pub.* No. 2 Gallery Press, Liverpool, p. 187–200.
Hartmann, W. K.: 1970, *Icarus* **12**, 131.
Harvie, R.: 1910, *Roy. Soc. Can. Trans. Ser. 3*, **3**, 249.
Holmes, A.: 1965, *Principles of Physical Geology*, Ronald Press Co. New York.
Jaffe, L. D.: 1965, *J. Geophys. Res.* **70**, 6129.
Johnson, S. W., Smith, J. A., Franklin, E. G., Moraska, L. K., and Teal, D. J.: 1969, *J. Geophys. Res.* **74**, 4838.
Kopal, Z.: 1970, *The Moon* **1**, 451.
Kozyrev, N. A.: 1959, *Priroda* **3**, 84.
Kozyrev, N. A.: 1963, *Nature* **198**, 979.
Kuiper, G. P.: 1965, Interpretation of Ranger VII Records: as cited by Hartman, 1970.
Lorenz, V.: 1970, *Geol. Soc. Amer. Bull.* **81**, 1823.
Lorenz, V., McBirney, A. R., and Williams, H.: 1970, 'An Investigation of Volcanic Depressions:

Part III, Maars, Tuff-Rings, and Diatremes', *NASA Progress Report*, 198 p.
Mason, B. and Melson, W. C.: 1970, *The Lunar Rocks*, Wiley-Interscience, New York, 178 p.
McCauley, J. F.: 1967, 'Geologic Results from the Lunar Precursor Probes': *AIAA 4th Annual Meeting and Technical Display*, No. 67–862.
McGetchin, T. R.: 1968, 'The Moses Rock Dike: Geology, Petrology and Mode of Emplacement of a Kimberlite Bearing Breccia Dike, San Juan County, Utah', Unpublished Ph.D. Thesis, California Institute of Technology.
McGetchin, T. R.: 1970, 'Mechanism of Emplacement of Kimberlite and Related Breccia at Moses Rock Dike, Utah', Abst. Upper Mantle Project Symposium, Flagstaff, Arizona, p. 6–7.
Middlehurst, B. M.: 1967, *Rev. Geophys.* **5**, 173.
Miller, G. H. and King, I. R.: 1966, 'An Experimental Study of Fluidization Processes Under Lunar Conditions': Natl. Aeronautics and Space Agency Contractor Rept. CR-627, 92 p.
Mills, A. A.: 1969, *Nature* **224**, 863.
Mitchell, J. K., Bromwell, L. G., Carrier III, W. D., Costes, N. C., and Scott, R. F.: 1972, *J. Geophys. Res.* **77**, 5641.
Murray, J. B. and Guest, J. E.: 1970, *Modern Geology* **1**, 149.
Oberbeck, V. R. and Quaide, W. L.: 1967, *J. Geophys. Res.* **72**, 4697.
Oberbeck, V. R. and Quaide, W. L.: 1968, *Icarus* **9**, 446.
O'Keefe, J. A. and Adams, E. W.: 1965, *J. Geophys. Res.* **70**, 3819.
Öpik, E. J.: 1971, in A. Kopal (ed.), *Adv. Astron. Astrophys.* **8**, 107.
Osborne, F. F. and Grimes-Graeme, R.: 1936, *Am. J. Sci., Ser. 5*, **32**, 43.
Pike, R. J.: 1968, 'Meteoritic Origin and Consequent Endogenic Modification of Large Lunar Craters – A Study in Analytical Geomorphology': Unpub. Ph.D. Thesis, University of Michigan, Ann Arbor, 404 p.
Pike, R. J.: 1972, 'Geometric Similitude of Lunar and Terrestrial Craters': Abst. IGC 24th Session, Section 15, p. 41–47.
Quaide, W. L. and Oberbeck, V. R.: 1968, *J. Geophys. Res.* **73**, 5247.
Reynolds, D. L.: 1954, *Amer. J. Sci.* **252**, 577.
Schumm, S. A. and Simmons, D. B.: 1969, *Science* **165**, 201.
Schumm, S. A.: 1970, *Geol. Soc. Amer. Bull.* **81**, 2539.
Shoemaker, E. M.: 1965, 'Preliminary Analysis of the Fine Structures of Mare Cognitum': as cited by Hartman, 1970.
Shoemaker, E. M., Batson, R. M., Holt, H. E., Morris, E. C., Rennilson, J. J., and Whitaker, E. A.: 1968, in *Surveyor VII A Preliminary Report*, NASA. SA-173, p. 50–53.
Shoemaker, E. M., Batson, R. M., Holt, H. E., Morris, E. C., Rennilson, J. J., and Whitaker, E. A.: 1969, *J. Geophys. Res.* **74**, 6081.
Short, N. M. and Forman, M. L.: 1969, *Modern Geology* **3**, 69.
Siegal, B. S.: 1971, 'Effect of Grain Size, "Regolith" Thickness, Gas Pressure, and Duration of Gas Streaming on the Morphology of Fluidization Craters', Unpub. M.S. Thesis, The Pennsylvania State University, 180 p.
Siegal, B. S. and Gold, D. P.: 1972, $E \oplus S$ **53**, 430.
Tyler, G. L.: 1968, *J. Geophys. Res.* **73**, 7609.
Watkins, J. S. and Kovach, R. L.: 1972, *Science* **175**, 1244.
White, J. W.: 1971, *J. Geophys. Res.* **76**, 8599.
Yokoyama, I.: 1957, *Earthquake Res. Inst.* **35**, 75.